Nano Research

Open Access

Research Article

Self-assembled SnS/TaS_2 superconducting superlattice with non-trivial band topology

Junjie Wu[1,§], Xiaoming Zhang[2,§], Tongrui Li[3,§], Chunsheng Wang[4,§], Changlong Wang[1], Yan Feng[1], Xiang Ma[1], Zhe Sun[3], Yalin Lu[1], Guolin Zheng[4], Feng Liu[5], and Bin Xiang[1] ✉

[1] *Department of Materials Science & Engineering, CAS Key Lab of Materials for Energy Conversion, Anhui Laboratory of Advanced Photon Science and Technology, University of Science and Technology of China, Hefei 230026, China*
[2] *College of Physics and Optoelectronic Engineering, Ocean University of China, Qingdao 266100, China*
[3] *National Synchrotron Radiation Laboratory, CAS Center for Excellence in Nanoscience, University of Science and Technology of China, Hefei 230029, China*
[4] *Anhui Key Laboratory of Low-Energy Quantum Materials and Devices, High Magnetic Field Laboratory, HFIPS, Chinese Academy of Sciences, Hefei 230031, China*
[5] *Department of Materials Science and Engineering, University of Utah, Salt Lake City, Utah 84112, USA*
§ *Junjie Wu, Xiaoming Zhang, Tongrui Li, and Chunsheng Wang contributed equally to this work.*

Cite this article: *Nano Research*, **2026**, *19*, 94907811. https://doi.org/10.26599/NR.2025.94907811

ABSTRACT: Intrinsic topological superconductors have garnered significant attention for their potential to harbor novel quantum phenomena. However, the limited availability of suitable material systems has hindered progress in this field. Here, we present the synthesis and characterization of high-quality self-assembled SnS/TaS_2 ($SnTaS_3$) superlattice, which exhibits superconductivity alongside non-trivial band topology. Temperature-dependent magnetization susceptibility and electrical transport results confirm $SnTaS_3$ as a type-II superconductor with a critical transition temperature T_c of 3 K. Interestingly, this superconductivity can be turned off via an innovative solid proton gate technique, and a new superconducting state with a T_c of ~ 2.3 K emerges when the gating voltage reaches −9.47 V. Heat capacity measurements reveal strong electronic correlations within this material, which is further supported by angle-resolved photoemission spectroscopy and first-principles calculations, underscoring the effect of topological flat bands and Van Hove singularity. Our research introduces a promising self-assembled material platform, adeptly positioned to delve into the quest for topological superconductors.

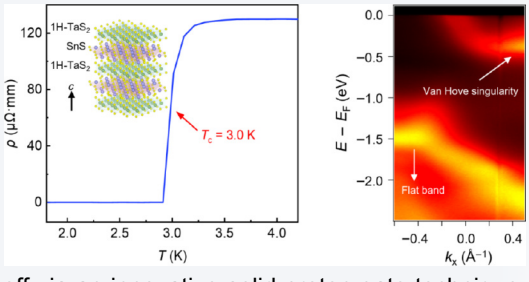

KEYWORDS: self-assembled, superconductivity, superlattice, band topology

1 Introduction

Topological superconductors have recently attracted considerable interest due to their potential for fault-tolerant quantum computing [1–4]. These materials provide a hint for the existence of Majorana fermions conceived from a zero-biased conduction peak, the quantized thermal conductivity, and the anomalous Josephson effect. The quest for realizing such phenomena is ongoing; notably due to the lack of intrinsic topological superconductors, a prevalent approach is to fabricate topological-insulator/superconductor heterostructures to induce extrinsically superconductivity in topological bound states via the proximity effect [5–8]. Unfortunately, the detection and manipulation of Majorana bound states in these heterostructures are frequently impeded by the contribution of nontopological bound states and the complications of material interfaces [3], which underscores the urgent need for intrinsic topological superconductor candidates.

In the search for intrinsic topological superconductors, materials exhibiting coexistence of non-trivial topology and superconductivity are considered as potential candidates [9]. One interesting avenue is the discovery of superconductivity in association with topological flat bands, as exemplified in the twisted graphene layers where flat bands and Van Hove singularities are found conducive to superconductivity and strongly correlated states [10, 11]. Studies have shown that flat bands can significantly increase both the coupling constant and the transition temperature (T_c) due to the increased density of states (DOS) at the Fermi level

Received: May 2, 2025; **Revised:** June 22, 2025
Accepted: July 17, 2025

✉Address correspondence to binxiang@ustc.edu.cn

(E_F) [12–14]. Besides, Van Hove singularity, a saddle point in the band structure, also leads to divergent DOS [15]. When E_F is close to such localized states, even weak interactions are magnified, giving rise to new phases of matter with desirable properties, such as superconductivity [11, 16]. Consequently, the design of superconductors with high T_c and electron-mediated pairing mechanisms coupled with non-trivial band topology is a focal point of interest [14, 17–22]. However, investigating the physical properties associated with non-trivial topology still remains challenging, as naturally the topological bands, such as flat bands, tend to be located far from E_F [23] or do not coexist with superconductivity [24].

In this paper, we report the coexistence of superconducting state and non-trivial band topology in $SnTaS_3$ superlattice synthesized via a modified chemical vapor transport (CVT) method. The self-assembled structure of $SnTaS_3$ was confirmed through X-ray diffraction (XRD), micro-Raman spectroscopy, high-resolution transmission electron microscopy (HRTEM), and electron diffraction pattern analysis. The superconducting state was established with a transition temperature T_c of 3 K, as determined by measurements of temperature-dependent magnetization susceptibility and electrical transport. Interestingly, this superconductivity can be switched off by using a solid proton gate technique, and a new superconducting state with a T_c of ~ 2.3 K is observed when the gating voltage is in the range of −9.47 to −9.72 V, which is attributed to the sign change of quantum electronic stress (QES) induced by charge carries. Heat capacity data revealed strong electronic correlation effects in $SnTaS_3$, which is supported by angle-resolved photoemission spectroscopy (ARPES) and first-principles calculations, further substantiating the presence of topological flat band and Van Hove singularity. This growth method is not only applicable to $SnTaS_3$ but also can be extended to the synthesis of $PbTaS_3$ superlattice, which exhibit similar features to $SnTaS_3$. Our work elucidates the significance of materials that possess both superconducting properties and non-trivial band topology, positioning them as crucial contenders in the pursuit of intrinsic topological superconductors.

2 Results and discussion

As shown in Fig. 1(a), the $SnTaS_3$ superlattice exhibits distinctive structural features, attributable to its alternating layers of monolayer SnS and TaS_2, which are formed through self-assembly (see Experimental section for details). The single-crystal XRD analysis of the as-grown $SnTaS_3$ superlattice (Fig. 1(b)), demonstrates sharp (00*l*) peaks, with the (004) plane peak at 12.6° and a full width at half maximum (FWHM) of 0.07° (Fig. 1(c)), indicating exceptional crystallinity. Powder XRD measurements (Fig. S1 in the Electronic Supplementary Material (ESM)) further confirm the absence of secondary phases and establish a lattice periodicity of 12.3 Å, which agreed well with the calculated value of 12.25 Å. The system is then structurally optimized with lattice constants of a = 23.34 Å, b = 5.83 Å, and c = 12.25 Å, indicating an orthorhombic structure with space group *Pmmm*. The molar ratio of Sn, Ta, and S in the as-grown superlattice was determined to be 1:1:3 through a combination of energy dispersive X-ray spectroscopy (EDS), X-ray photoelectron spectroscopy (XPS), and X-ray fluorescence spectroscopy (XRF) analyses (Figs. S2 and S3 and Tables S1 and S2 in the ESM). EDS mapping elucidates a uniform distribution of Sn, Ta, and S throughout the superlattice (Fig. S4 in the ESM). The combined results demonstrate the high-quality crystal structure of the as-grown $SnTaS_3$ superlattice.

To delineate the interactions within $SnTaS_3$ superlattice and its constituent subsystems, micro-Raman spectroscopy and electron diffraction analysis were conducted. Figure 1(d) illustrates three distinct Raman peaks at approximately 93, 204, and 304 cm^{-1}, corresponding to the representative A_g^1 and A_g^3 vibrational modes of SnS and the E_{2g}^1 mode of TaS_2 layer, respectively. The peak positions, critical for determining layer count in such materials, are consistent with those reported in monolayer SnS and TaS_2 [25–28], indicating the monolayer composition of the alternating layers in our superlattice. Electron diffraction pattern offers further insights into the alternating monolayered structure of $SnTaS_3$, revealing two sets of lattice diffraction spots that highlight the complexity of the self-assembled superlattice [28]. The green and yellow circles in the pattern (Fig. 1(e)) denote diffraction spots from the SnS and TaS_2 sublattices, respectively, corroborating the simulated results depicted in Fig. 1(f). The HRTEM image (Fig. S5 in the ESM) discloses a well-ordered atomic arrangement on the surface of $SnTaS_3$, with a lattice spacing of 0.28 nm corresponding to the (100) plane. A cross-sectional high-angle annular dark-field scanning transmission electron microscopy (HAADF-STEM) image of the superlattice (Figs. 1(g) and 1(h)), with an overlaid structural model, confirms the alternating stacking of monolayer SnS and TaS_2 layers. The interlayer distance between adjacent TaS_2 layers, determined to be 12.3 Å, is consistent with XRD findings. These observations provide compelling evidence for the alternating layers of monolayer SnS and TaS_2 in our self-assembled superlattice, contrasting with the reported misfit compounds [29]. The layers, together by van der Waals forces, allow for the mechanical exfoliation of $SnTaS_3$ into stable flakes (Fig. 1(i)). This characteristic renders the material an excellent substrate for exploring the properties of $SnTaS_3$ and their applications in device fabrication.

To investigate the superconductivity properties of $SnTaS_3$, we conducted electrical transport measurements, as schematically illustrated in Fig. 2(a). The temperature-dependent resistivity (Fig. 2(b)) exhibits a metallic behavior as the resistivity drops from 300 to 6 K. To better predict the resistivity contribution from electron–phonon interactions in this metallic region of our sample, we employ the parallel resistor model [30–38], which predicts a temperature-dependent resistivity, as given by

$$\rho(T) = \left[\frac{1}{\rho_{sat}} + \frac{1}{\rho_{ideal}(T)}\right]^{-1} \quad (1)$$

where ρ_{sat} is the saturated resistivity at high temperature, and $\rho_{ideal}(T)$ can be written as $\rho_{ideal}(T) = \rho_0 + \rho_{i,L}(T)$. Here ρ_0 is the temperature-independent residual resistivity arising from impurity scattering, and $\rho_{i,L}(T)$ can be defined by Wilson's theory as [34, 39]

$$\rho_{i,L}(T) = C\left(\frac{T}{\theta_D}\right)^r \int_0^{\frac{\theta_D}{T}} \frac{x^r}{(e^x - 1)(1 - e^{-x})} dx \quad (2)$$

where θ_D denotes Debye temperature, and C is the material-dependent constant. After fitting with r = 3, the residual resistivity value ρ_0 = 0.13 mΩ·mm is extracted. Furthermore, the temperature derivative of the resistivity of $SnTaS_3$ does not reveal any charge density wave transition (inset of Fig. 2(b)) [35]. The resistivity in the superconducting region is detailed in Fig. 2(c), where a sharp drop at T_c = 3 K is indicative of superconductivity (T_c is defined as the 50% resistance of the normal state). Figures 2(d) and 2(e) illustrate the temperature-dependent resistance transition curves under

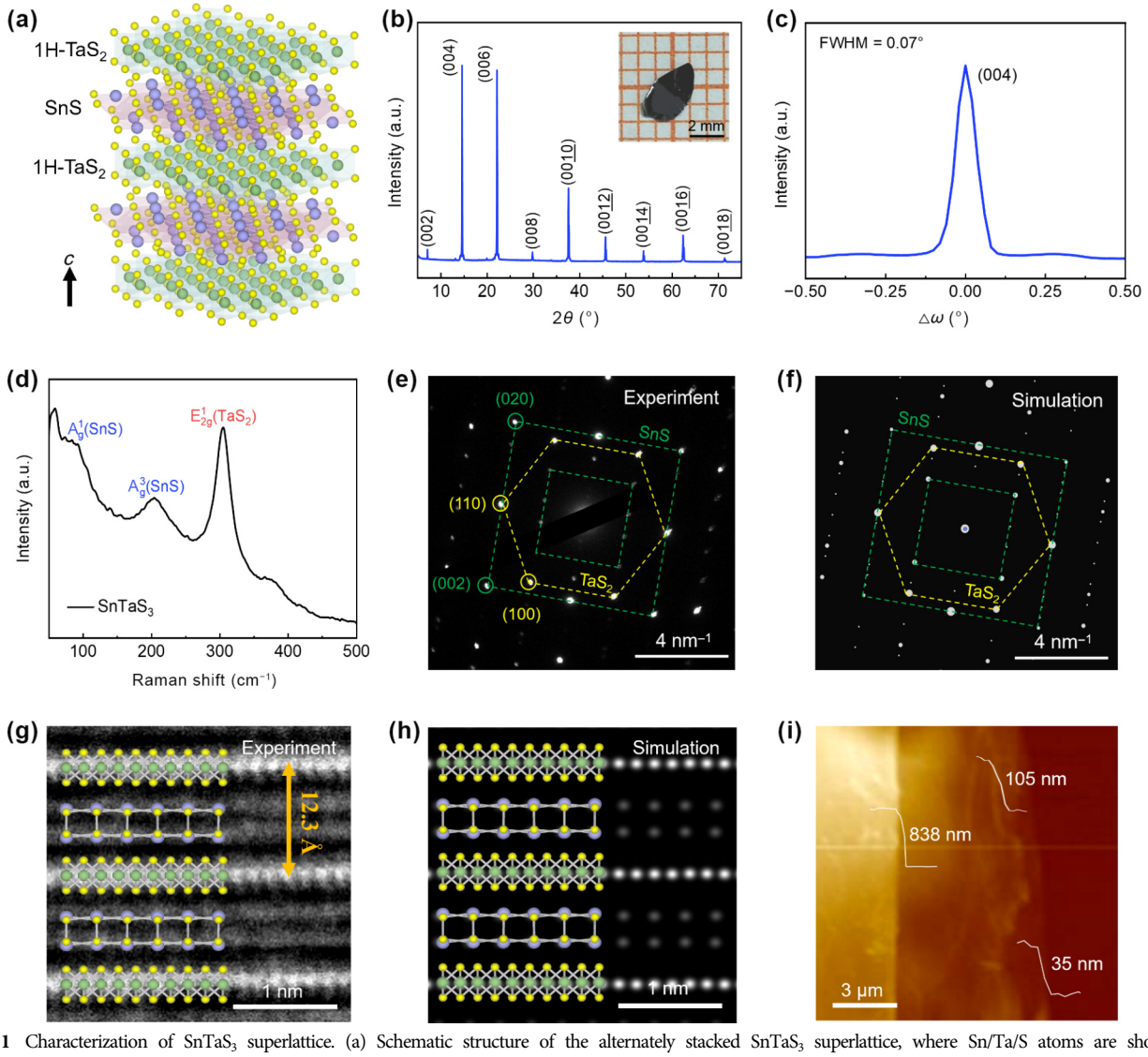

Figure 1 Characterization of $SnTaS_3$ superlattice. (a) Schematic structure of the alternately stacked $SnTaS_3$ superlattice, where Sn/Ta/S atoms are shown in purple/green/yellow, respectively. (b) XRD spectrum of $SnTaS_3$ single crystal with (00*l*) reflections. The set shows the optical image of $SnTaS_3$ sample. (c) The rocking curve of $SnTaS_3$ single crystal. (d) Raman spectrum of $SnTaS_3$ single crystal. (e) and (f) Electron diffraction pattern and the corresponding simulated image. (g) and (h) HAADF-STEM image and the corresponding simulated image. (i) AFM image of the mechanically-exfoliated $SnTaS_3$ nanosheets.

various magnetic fields, applied parallel or perpendicular to the *ab*-plane, respectively. The superconducting transition is broadened by the application of a magnetic field and shifts to lower temperatures with the increasing field strength. The upper critical field H_{c2} as a function of temperature for both field orientations (Figs. 2(f) and 2(g)) show a linear relationship with T_c, which can be described by the three-dimensional (3D) Ginzburg–Landau (GL) theory [40–42]

$$H_{c2}^{\perp}(T) = \frac{\Phi_0}{2\pi\xi_{//}^2(0)}\left(1-\frac{T}{T_c}\right) \quad (3)$$

$$H_{c2}^{//}(T) = \frac{\Phi_0}{2\pi\xi_{//}(0)\,\xi_{\perp}(0)}\left(1-\frac{T}{T_c}\right) \quad (4)$$

where $\Phi_0 = \frac{h}{2e}$ is the magnetic flux quantum, $\xi_{//}(0)$ and $\xi_{\perp}(0)$ are the zero-temperature GL coherence length in and out of the *ab* plane, respectively. The linear extrapolation of this relationship provides the zero-temperature upper critical fields $H_{c2}^{\perp}(0)$ = 0.45 T and $H_{c2}^{//}(0)$ = 4.51 T. These values are below the Pauli paramagnetic limit H_P ($H_P = 1.86T_c$ = 5.58 T) [43], which implies that TaS_2 is not fully isolated, allowing Cooper pairs to penetrate through SnS interlayers. The zero-temperature Ginzburg–Landau coherence lengths are determined to be $\xi_{//}(0)$ = 27.19 nm and $\xi_{\perp}(0)$ = 2.69 nm, respectively. Additionally, the Hall resistivity of $SnTaS_3$ is positive, linearly dependent on the magnetic field up to 7 T, and exhibits a temperature-dependent Hall coefficient without carrier sign change (Fig. S6 in the ESM). The temperature dependence of the magnetization, measured during zero-field cooling (ZFC) and field-cooling (FC) processes, is displayed in Fig. 2(h). The discrepancy between the ZFC and FC curves suggests that $SnTaS_3$ displays a type-II superconductor [44]. In our sample, the largest superconducting volume fraction was estimated to be close to 100%. The T_c, as derived from the susceptibility curve, is ~ 3 K, in agreement with the transport measurement. The magnetization versus magnetic field relationship is measured at 2 K, with the field applied parallel to the *c*-axis (Fig. 2(i)), showing a distinct hysteresis loop. These findings further support the superconducting nature of $SnTaS_3$. It is worth noting that our

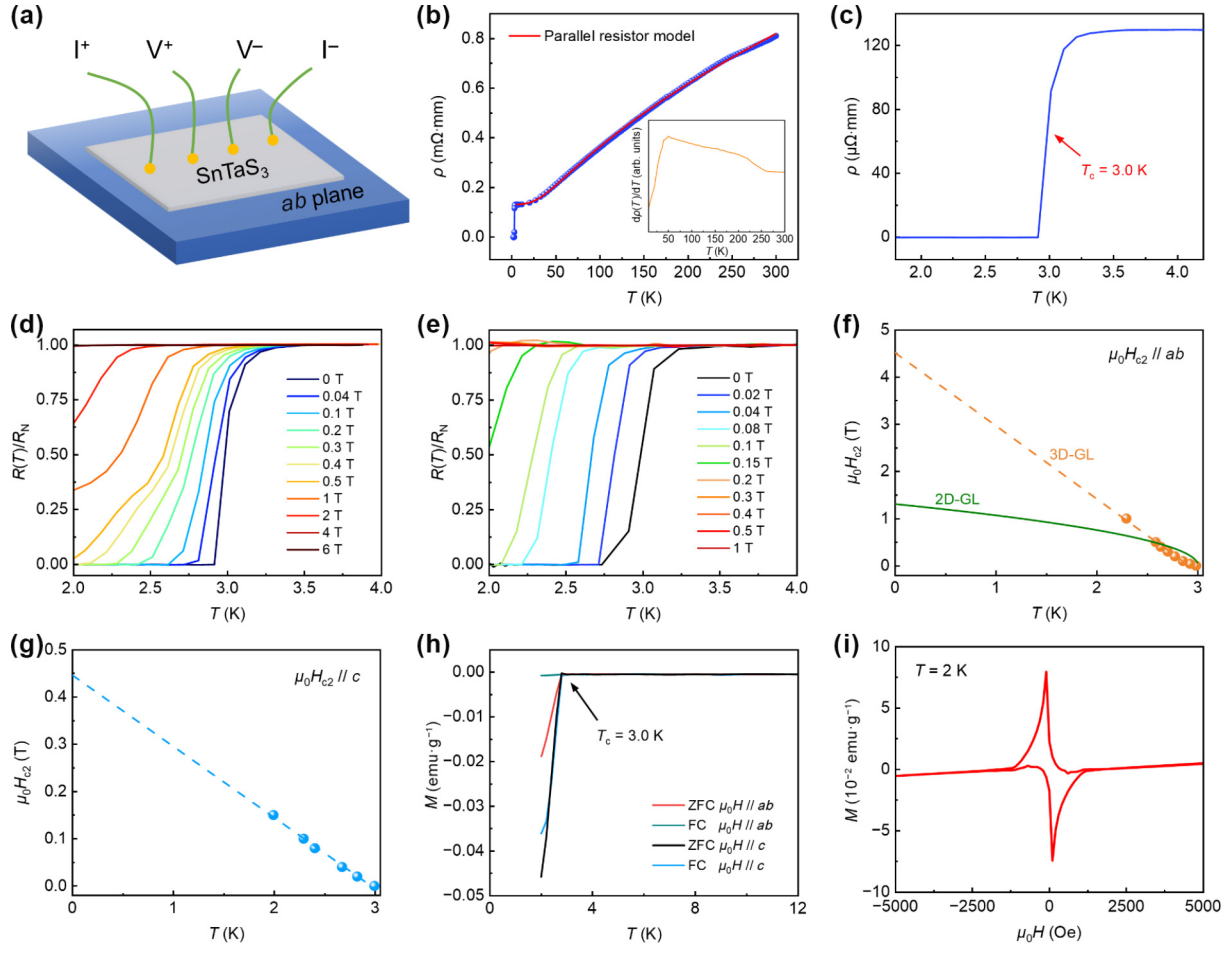

Figure 2 Superconductivity of $SnTaS_3$ superlattice. (a) Schematic diagram of electrical transport measurement. (b) Temperature-dependent electrical resistivity at zero field fitted with the parallel resistor model. The inset shows temperature derivative of resistivity. (c) A zoomed view of the zero drop transition of resistivity in the superconducting region of (b). (d) and (e) The low-temperature in-plane resistance $R(T)$ curves of $SnTaS_3$ under different magnetic fields for $H_{c2}//ab$ (d) and $H_{c2}//c$ (e), respectively. R_N is defined as the resistance of normal state. (f) and (g) Temperature dependence of the upper critical field extracted from the $R(T)$ curves with $H_{c2}//ab$ (f) and $H_{c2}//c$ (g). (h) Temperature dependence of the magnetization (M–T curve) of the superlattice under magnetic field of 50 Oe for ZFC and FC processes. (i) The isothermal magnetization curve (M–H curve) at 2 K.

$SnTaS_3$ sample maintains its crystalline structure and superconducting properties under ambient conditions for an extended period of up to two weeks, corroborated by XRD and transport measurements (Fig. S7 in the ESM). This long-term stability suggests that SnS layers have provided effective protection for the active TaS_2 layers [45], to preserve the superconducting properties of the whole superlattice. Furthermore, a brief comparison with other TaS_2-based superlattices or misfit compounds would further highlight the uniqueness of the SnS layer within $SnTaS_3$ (Table S3 in the ESM).

We then introduce a protonic gate technique to achieve electrical control over the superconductivity in $SnTaS_3$. Figure 3(a) depicts a solid proton gate device [46–49], where a voltage is applied between the platinum gate electrode and $SnTaS_3$ nanoflake, promoting proton intercalation (see S10 in the ESM for details). Figure 3(b) presents the temperature-dependent resistance of a 30 nm thick $SnTaS_3$ nanoflake under various gate voltages. At a gate voltage (V_g) of 0 V, the pristine superconducting transition is observed around 2.8 K, due to the high DOS of flat bands near E_F. Upon increasing V_g to −1.52 V, no discernible change is observed in superconducting transition of this system. Further increasing V_g induces an elevated carrier density through protonic intercalation, resulting in a loss of superconductivity within the range of our experimental measurements. Intriguingly, from −9.47 to −9.72 V, a new superconducting state with a T_c of about 2.3 K emerges. To understand this intriguing behavior, it is important to note the arch behavior of hole density (n) with different V_g values (Fig. 3(c)). The increase region in the n–V_g curve stems from the injection of protons (H^+), and the decrease region is due to the charge transfer between sulfur and hydrogen, leading to the injection of electrons (H^-) into the system [46, 48]. Based on the changes in T_c with different n, the mechanism of QES induced by carrier doping is considered. QES is a non-mechanical phenomenon that generates lattice stress solely through electronic excitation and perturbation [50, 51]. It follows a quantum version of Hooke's law

$$\sigma^{QE} = \frac{\partial \mu}{\partial \varepsilon_{ij}} \Delta n \tag{5}$$

where $\frac{\partial \mu}{\partial \varepsilon_{ij}}$ represents the electron deformation potential with $\mu = E_F$ for metal and ε_{ij} is the lattice strain; Δn is the change of carrier density. One of the most interesting aspects of QES is that it can be either tensile (positive) or compressive (negative), depending on the sign of Δn. Specifically, electron doping induces a compressive

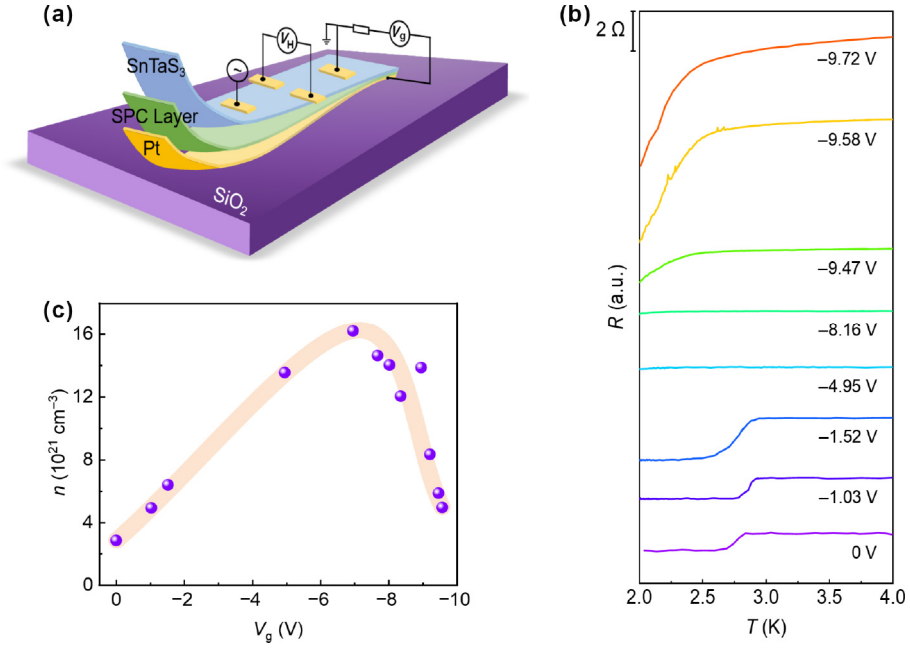

Figure 3 Protonic gating modulation of a $SnTaS_3$ nanoflake. (a) The schematic diagram of a $SnTaS_3$ solid proton conductor (SPC) device, where a $SnTaS_3$ flake lies on the solid proton conductor and a Pt electrode is utilized as the backgate electrode. (b) Temperature dependence of resistance with different gate values. (c) The gate voltage dependent hole density curve.

QES, while hole doping induces a tensile QES. This implies that one might be able to apply a tensile QES, which naturally gives rise to a nonzero internal positive pressure, instead of applying external higher pressure, to a superconductor like our $SnTaS_3$ sample through hole doping, thereby observing the change in T_c. Moreover, a high T_c requires a large electronic density of states at the Fermi level and a significant electron–phonon coupling [52–54]. In our experiments, when V_g is less than −9.47 V in $SnTaS_3$, significant hole doping, compared to the scenario at V_g = 0 V, suppresses T_c via a tensile QES without inducing a phase transition, resulting in a diminished or entirely absent superconducting state. This can be understood by the decrease in electronic density of states and electron–phonon coupling based on our QES analysis. Conversely, when V_g exceeds −9.47 V, a reduced n engenders an internal compressive QES, leading to the re-occurrence of T_c at ~ 2.3 K. Overall, the tunability of T_c likely arises from the interplay among the QES-modified phonon frequency, electronic density of states, and electron–phonon coupling [51]. Our discovery successfully reinforces the role of QES on superconductivity.

Figure 4(a) showcases specific heat capacity measurements, depicted as C_p/T versus T^2, under out-of-plane magnetic fields of 0 and 1 T. A distinct anomaly in the specific heat curve at approximately 2.9 K corroborates the T_c observed in electrical transport results. However, this anomaly disappears under a 0.5 T field, suggesting an upper critical field H_{c2} not exceeding 0.5 T, consistent with resistivity data (Fig. 2(g)). Given that the measured specific heat encompasses both electronic and lattice contributions, the Sommerfeld coefficient (γ) is extracted from the linear regression of $C_p/T = \gamma + \beta T^2$ [34]. The resulting value is γ = 51.77 mJ·mol^{-1}·K^{-2}, which surpasses that of pristine TaS_2 (8.5 mJ·mol^{-1}·K^{-2}) and its intercalated compounds (7.4–9.5 mJ·mol^{-1}·K^{-2}) [55]. To investigate possible origins of such giant and unusual γ, we perform first-principles calculations of band structures and the projected DOS for $SnTaS_3$ (Fig. 4(d) and Figs. S8 and S9 in the ESM). Interestingly, localized flat bands near the Γ point, which are close to the E_F, and an elevated PDOS at E_F is observed in $SnTaS_3$. These features suggest a link between the enhanced γ value and strong electronic correlations due to these non-trivial topological bands. Moreover, a Van Hove singularity at ~ 0.5 eV and a flat band at ~ 1.5 eV below the E_F near the Γ point are identified, corresponding to a significant peak in the PDOS in that region. We subsequently conduct ARPES measurements at 10 K with 23 eV photon energy to validate these theoretical calculations. The measured Fermi surface and energy band dispersions along the high-symmetry directions (Figs. 4(b) and 4(c) and Fig. S10 in the ESM) are presented. Although the flat bands near E_F are not discernible due to experimental resolution and detection limitations, the flat bands at ~ 1.5 eV below E_F are clearly detected in both the Γ–K and Γ–M directions. Furthermore, Van Hove singularity at ~ 0.5 eV below E_F located at the M point, are also observed. It is noted that the energy bands in ARPES experiments align well with our theoretical calculations. After incorporating spin-orbit coupling (SOC) into theoretical calculations (Fig. 4(e)), the splitting of spin degeneracy occurs due to broken inversion symmetry. However, topological flat bands and Van Hove singularity, irrespective of their distance from E_F, remain unchanged.

The self-assembled superlattice under discussion has significantly enriched the fundamental physics and the intriguing properties associated with layered materials. This concept can be readily extended to other TaS_2-based layered materials, such as the $PbTaS_3$ superlattice (Figs. S11–S17 and Table S4 in the ESM). $PbTaS_3$ superlattice, which consists of alternating monolayers of PbS and TaS_2, exhibits a crystal and electronic band structure analogous to that of $SnTaS_3$, and importantly, has also a T_c of ~3 K. The same order of T_c in $PbTaS_3$ and $SnTaS_3$ points to the primary role of monolayer TaS_2 in mediating superconductivity [56], while the semiconductor layer AS (where A = Sn, Pb) acts as an ideal protection layer for superconductivity. Therefore, our work

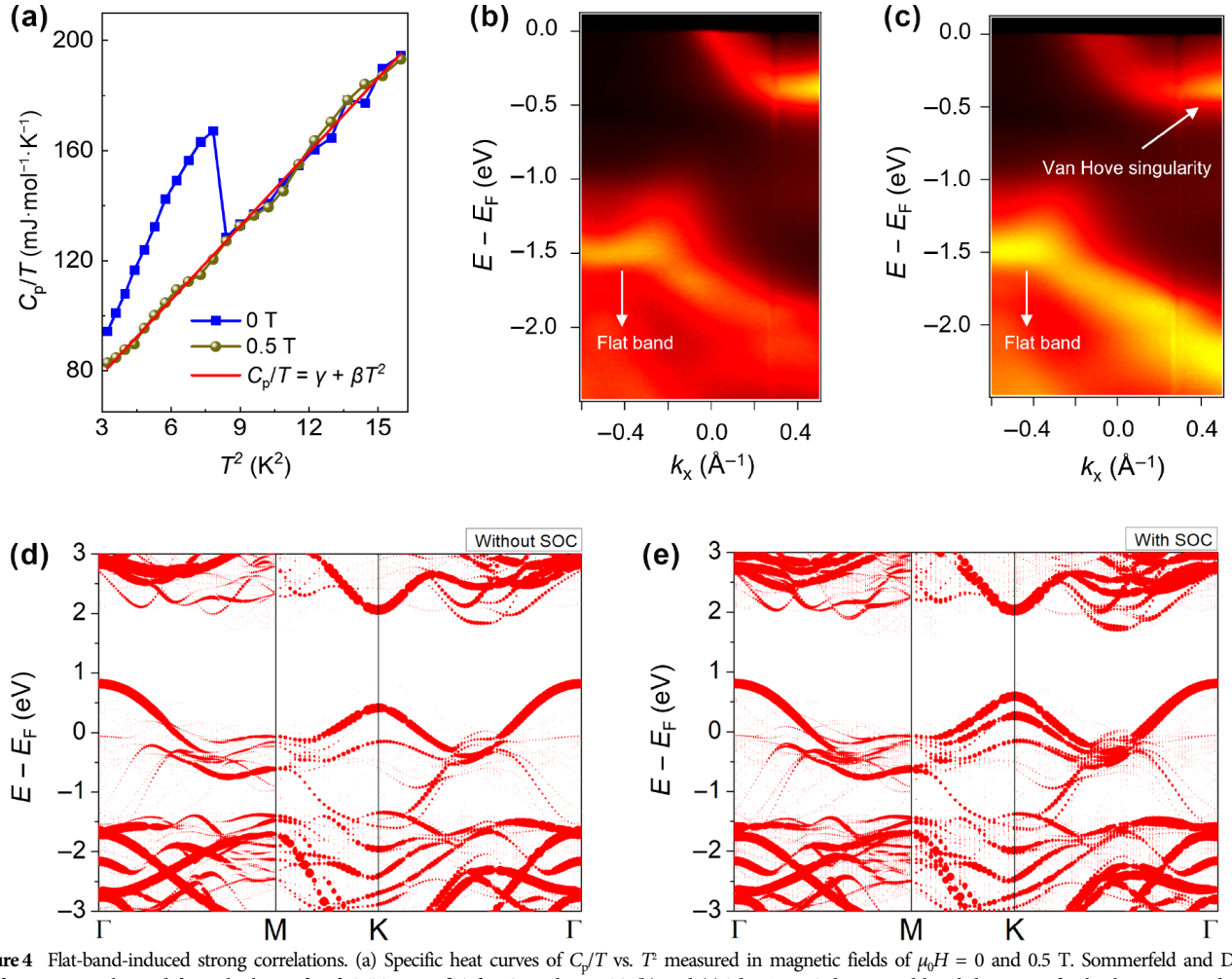

Figure 4 Flat-band-induced strong correlations. (a) Specific heat curves of C_p/T vs. T^2 measured in magnetic fields of $\mu_0 H$ = 0 and 0.5 T. Sommerfeld and Debye coefficients were obtained from the linear fit of $C_p/T = \gamma + \beta T^2$ for C_p under 0.5 T. (b) and (c) The ARPES-determined band dispersion for k_x along Γ–K and Γ–M directions measured with 23 eV photon energy, at 10 K. (d) and (e) The calculated band structure of $SnTaS_3$ without/with SOC, where the magnitude of red dots was drawn proportionally to the weight of electronic states after unfolding into the Brillouin zone of TaS_2 primitive cell.

provides an important methodology for creating self-assembled superlattices in order to retain the two-dimensional (2D) superconductivity of the constituent layers.

3 Conclusions

In summary, we report the coexistence of superconductivity and non-trivial band topology in self-assembled $SnTaS_3$ superlattice, synthesized through an optimized chemical vapor transport method. This approach is readily extendable to the synthesis of $PbTaS_3$ superlattice, which exhibit analogous crystal and band structures. The superconducting properties in $SnTaS_3$ are substantiated by temperature-dependent measurements of magnetic susceptibility and electrical transport. Notably, this superconductivity can be modulated via a solid proton gate technique, leading to the re-entrance of a new superconducting state with a T_c of ~ 2.3 K, which is attributed to the effect of tensile QES induced by hole doping. Heat capacity measurements, combined with ARPES and theoretical calculations, demonstrate strong electronic correlations in $SnTaS_3$, indicating the significant impact of topological flat bands and Van Hove singularity. Our findings underline a synergy between superconductivity and nontrivial topological band structures in $ATaS_3$ (A = Sn, Pb), suggesting these materials as promising candidates for intrinsic topological superconductors.

4 Experimental section

4.1 Single-crystal growth

High-quality $SnTaS_3$ and $PbTaS_3$ single crystals were synthesized via a modified CVT method. High purity tin/lead powder (Alfa Aesar, 99.999%), tantalum powder (Alfa Aesar, 99.999%), and sulfur powder (Alfa Aesar, 99.999%) were ground together in a non-stoichiometric ratio 1:3:6, sealed with iodine (or/and corresponding metal halides) as the transport agent in a vacuum-sealed quartz tube. The tube was then placed in a two-zone furnace (1223 to 1073 K), held for several days. After cooling to room temperature, the single crystals were obtained. Notably, the non-stoichiometric chemical composition of the source materials and the one-step method were key to obtaining our single crystals.

4.2 Sample characterizations

The XRD patterns were collected from a diffractometer using Cu Kα (λ = 1.5418 Å) radiation to reveal the interlayer spacings of the samples. Raman spectroscopic measurements were performed at

room temperature (Renishaw inVia Qontor) with laser excitation at 532 nm. HRTEM and electron diffraction were characterized using FEI Talos F200X. The thickness of the exfoliated superlattice nanosheets was characterized by atomic force microscopy (AFM, Bruker Multimode 8 and DIMENSION FastScan). Magnetization characterizations were measured using a SQUID magnetometer (MPMS-3, Quantum Design). Electrical transport measurements were carried out using a physical property measurement system (PPMS-14 T, Quantum Design). The ARPES measurements were performed at beamline 13 U of the National Synchrotron Radiation Laboratory at Hefei, China, with a Scienta Omicron DA30L analyzer. The overall energy resolution is better than 20 meV, and the angular resolution is 0.3°. Single crystal samples were cleaved in ultrahigh vacuum better than 5×10^{-10} mbar to achieve clean surfaces, and ARPES measurements were performed using spolarized photons at sample temperature ~ 10 K.

4.3 Theoretical calculations

First-principles calculations were performed by using Vienna *ab initio* simulation package (VASP) based on the density functional theory (DFT) [57, 58]. The Perdew–Burke–Ernzerhof (PBE)-type exchange correlation functional [59] and the projector augmented wave method [60] were employed for pseudopotentials and the energy cutoff was set to 500 eV. The crystal structure of $SnTaS_3$ was fully optimized without considering SOC effect until energy and force were respectively converged with an accuracy of 10^{-5} eV and 0.01 eV·Å^{-1}. The uniform $1 \times 2 \times 4$ k-point mesh was sampled in Brillouin zone. van der Waals correction was included and described by optPBE-vdW functionals [61]. Self-consistent calculations were performed with considering SOC effect, and the unfolded band structures along high-symmetry directions were obtained by using VASPKIT [62] to analyze the raw data produced by the VASP code. Similar method was applied to the first-principles calculations on $PbTaS_3$.

Electronic Supplementary Material: Supplementary material (powder XRD measurements of $SnTaS_3$; EDS, XPS, XRF, and EDS mapping of $SnTaS_3$; HRTEM image; Hall resistivity; sample stability; solid proton gate technique; theoretical calculations details; ARPES of $SnTaS_3$; XRD and XPS of $PbTaS_3$; electrical transport details; theoretical calculations; EDS, EDS mapping, and XRF of $PbTaS_3$; XRD comparison of $PbTaS_3$ and $SnTaS_3$; magneto-electrical transport; PDOS of $PbTaS_3$) is available in the online version of this article at https://doi.org/10.26599/NR.2025.94907811.

Data availability

All data needed to support the conclusions in the paper are presented in the manuscript and the Electronic Supplementary Material. Additional data related to this paper may be requested from the corresponding author upon request.

Acknowledgements

This work was supported by Innovation Program for Quantum Science and Technology (No. 2021ZD0302800), the National Natural Science Foundation of China (Nos. 52373309 and 12004357), and the National Key R&D Program of China (No. 2023YFA1610100). F. L. acknowledges the financial support from U.S. Department of Energy Office of Science-The Basic Energy Sciences program (DOE-BES) (No. DE-FG02-04ER46148). X. M. Z. acknowledges the financial support from the National Natural Science Foundation of China (No. 12574210). This research was partially carried out at the Instruments Center for Physical Sciences, the USTC Center for Micro and Nanoscale Research and Fabrication.

Declaration of competing interest

The authors declare no competing financial interest.

Author contribution statement

J. J. W., X. M. Z., T. R. L., C. S. W., and B. X.: Data curation, project administration, validation, writing manuscript, experimental design. C. S. W., Y. F., X. M., Z. S., Y. L. L., and G. L. Z.: Project administration, writing manuscript. X. M. Z., F. L., and B. X.: Project administration, funding acquisition, writing manuscript. All the authors have approved the final manuscript.

Use of AI statement

None.

References

[1] Kitaev, A. Y. Fault-tolerant quantum computation by anyons. *Ann. Phys.* **2003**, *303*, 2–30.

[2] Nayak, C.; Simon, S. H.; Stern, A.; Freedman, M.; Das Sarma, S. Non-abelian anyons and topological quantum computation. *Rev. Mod. Phys.* **2008**, *80*, 1083–1159.

[3] Wang, D. F.; Kong, L. Y.; Fan, P.; Chen, H.; Zhu, S. Y.; Liu, W. Y.; Cao, L.; Sun, Y. J.; Du, S. X.; Schneeloch, J. et al. Evidence for Majorana bound states in an iron-based superconductor. *Science* **2018**, *362*, 333–335.

[4] Sharma, M. M.; Sharma, P.; Karn, N. K.; Awana, V. P. S. Comprehensive review on topological superconducting materials and interfaces. *Supercond. Sci. Tech.* **2022**, *35*, 083003.

[5] Wang, M. X.; Liu, C. H.; Xu, J. P.; Yang, F.; Miao, L.; Yao, M. Y.; Gao, C. L.; Shen, C. Y.; Ma, X. C.; Chen, X. et al. The coexistence of superconductivity and topological order in the Bi_2Se_3 thin films. *Science* **2012**, *336*, 52–55.

[6] Banerjee, A.; Sundaresh, A.; Ganesan, R.; Kumar, P. S. A. Signatures of topological superconductivity in bulk-insulating topological insulator $BiSbTe_{1.25}Se_{1.75}$ in proximity with superconducting $NbSe_2$. *ACS Nano* **2018**, *12*, 12665–12672.

[7] Huang, C.; Zhou, B. T.; Zhang, H. Q.; Yang, B. J.; Liu, R.; Wang, H. W.; Wan, Y. M.; Huang, K.; Liao, Z. M.; Zhang, E. Z. et al. Proximity-induced surface superconductivity in Dirac semimetal Cd_3As_2. *Nat. Commun.* **2019**, *10*, 2217.

[8] Li, C. Q.; Zhao, Y. F.; Vera, A.; Lesser, O.; Yi, H. M.; Kumari, S.; Yan, Z. J.; Dong, C. Y.; Bowen, T.; Wang, K. et al. Proximity-induced superconductivity in epitaxial topological insulator/graphene/gallium heterostructures. *Nat. Mater.* **2023**, *22*, 570–575.

[9] Wang, Z. F.; Zhang, H. M.; Liu, D. F.; Liu, C.; Tang, C. J.; Song, C. L.; Zhong, Y.; Peng, J. P.; Li, F. S.; Nie, C. N. et al. Topological edge states in a high-temperature superconductor FeSe/$SrTiO_3$(001) film. *Nat. Mater.* **2016**, *15*, 968–973.

[10] Cao, Y.; Fatemi, V.; Fang, S. A.; Watanabe, K.; Taniguchi, T.; Kaxiras, E.; Jarillo-Herrero, P. Unconventional superconductivity in magic-angle graphene superlattices. *Nature* **2018**, *556*, 43–50.

[11] Li, G. H.; Luican, A.; Lopes dos Santos, J. M. B.; Castro Neto, A. H.;

Reina, A.; Kong, J.; Andrei, E. Y. Observation of van hove singularities in twisted graphene layers. *Nat. Phys.* **2010**, *6*, 109–113.
[12] Kopnin, N. B.; Heikkilä, T. T.; Volovik, G. E. High-temperature surface superconductivity in topological flat-band systems. *Phys. Rev. B* **2011**, *83*, 220503.
[13] Yin, J. X.; Zhang, S. S.; Chang, G. Q.; Wang, Q.; Tsirkin, S. S.; Guguchia, Z.; Lian, B.; Zhou, H. B.; Jiang, K.; Belopolski, I. et al. Negative flat band magnetism in a spin-orbit-coupled correlated kagome magnet. *Nat. Phys.* **2019**, *15*, 443–448.
[14] Tian, H.; Tu, T.; Jin, X. L.; Li, C. Y.; Lin, T.; Dong, Q.; Jing, X. L.; Liu, B.; Liu, R.; Li, D. et al. Tuning the flat band in Bi_2O_2Se by pressure to induce superconductivity. *J. Am. Chem. Soc.* **2024**, *146*, 7324–7331.
[15] Van Hove, L. The occurrence of singularities in the elastic frequency distribution of a crystal. *Phys. Rev.* **1953**, *89*, 1189–1193.
[16] Kohn, W.; Luttinger, J. M. New mechanism for superconductivity. *Phys. Rev. Lett.* **1965**, *15*, 524–526.
[17] Jin, K. H.; Huang, H. Q.; Mei, J. W.; Liu, Z.; Lim, L. K.; Liu, F. Topological superconducting phase in high-T_c superconductor MgB_2 with Dirac-nodal-line fermions. *npj Comput. Mater.* **2019**, *5*, 57.
[18] Zhou, X. Q.; Gordon, K. N.; Jin, K. H.; Li, H. X.; Narayan, D.; Zhao, H. D.; Zheng, H.; Huang, H. Q.; Cao, G.; Zhigadlo, N. D. et al. Observation of topological surface states in the high-temperature superconductor MgB_2. *Phys. Rev. B* **2019**, *100*, 184511.
[19] Balents, L.; Dean, C. R.; Efetov, D. K.; Young, A. F. Superconductivity and strong correlations in moiré flat bands. *Nat. Phys.* **2020**, *16*, 725–733.
[20] Peri, V.; Song, Z. D.; Bernevig, B. A.; Huber, S. D. Fragile topology and flat-band superconductivity in the strong-coupling regime. *Phys. Rev. Lett.* **2021**, *126*, 027002.
[21] Tian, H. D.; Gao, X. S.; Zhang, Y. X.; Che, S.; Xu, T. Y.; Cheung, P.; Watanabe, K.; Taniguchi, T.; Randeria, M.; Zhang, F. et al. Evidence for Dirac flat band superconductivity enabled by quantum geometry. *Nature* **2023**, *614*, 440–444.
[22] Pyykkönen, V. A.; Peotta, S.; Törmä, P. Suppression of nonequilibrium quasiparticle transport in flat-band superconductors. *Phys. Rev. Lett.* **2023**, *130*, 216003.
[23] Sethi, G.; Xia, B. W.; Kim, D.; Liu, H.; Li, X. Y.; Liu, F. Graph theorem for chiral exact flat bands at charge neutrality. *Phys. Rev. B* **2024**, *109*, 035140.
[24] Huang, H.; Zheng, L. X.; Lin, Z. Y.; Guo, X.; Wang, S.; Zhang, S.; Zhang, C.; Sun, Z.; Wang, Z. F.; Weng, H. M. et al. Flat-band-induced anomalous anisotropic charge transport and orbital magnetism in Kagome metal CoSn. *Phys. Rev. Lett.* **2022**, *128*, 096601.
[25] Tamalampudi, S. R.; Lu, J. Y.; Rajput, N.; Lai, C. Y.; Alfakes, B.; Sankar, R.; Apostoleris, H.; P. Patole, S. ; Almansouri, I.; Chiesa, M. Superposition of semiconductor and semi-metal properties of self-assembled 2D $SnTiS_3$ heterostructures. *npj 2D Mater. Appl.* **2020**, *4*, 23.
[26] Lin, D. J.; Li, S. C.; Wen, J. S.; Berger, H.; Forró, L.; Zhou, H. B.; Jia, S.; Taniguchi, T.; Watanabe, K.; Xi, X. X. et al. Patterns and driving forces of dimensionality-dependent charge density waves in 2H-type transition metal dichalcogenides. *Nat. Commun.* **2020**, *11*, 2406.
[27] Valencia-Ibáñez, S.; Jiménez-Guerrero, D.; Salcedo-Pimienta, J. D.; Vega-Bustos, K.; Cárdenas-Chirivi, G.; López-Manrique, L.; Herrera-Vasco, E.; Galvis, J. A.; Hernández, Y.; Giraldo-Gallo, P. Raman spectroscopy of few-layers TaS_2 and Mo - doped TaS_2 with enhanced superconductivity. *Adv. Electron. Mater.* **2022**, *8*, 2200457.
[28] Huang, S. T.; Bai, J. H.; Long, H. Y.; Yang, S. C.; Chen, W. W.; Wang, Q. Y.; Sa, B.; Guo, Z. Y.; Zheng, J. Y.; Pei, J. J. et al. Thermally activated photoluminescence induced by tunable interlayer interactions in naturally occurring van der Waals superlattice SnS/TiS_2. *Nano Lett.* **2024**, *24*, 6061–6068.
[29] Sankar, R.; Peramaiyan, G.; Panneer Muthuselvam, I.; Wen, C. Y.; Xu, X. F.; Chou, F. C. Superconductivity in a misfit layered $(SnS)_{1.15}(TaS_2)$ compound. *Chem. Mater.* **2018**, *30*, 1373–1378.
[30] Wiesmann, H.; Gurvitch, M.; Lutz, H.; Ghosh, A.; Schwarz, B.; Strongin, M.; Allen, P. B.; Halley, J. W. Simple model for characterizing the electrical resistivity in A-15 superconductors. *Phys. Rev. Lett.* **1977**, *38*, 782–785.
[31] Ziman, J. M. *Electrons and Phonons: The Theory of Transport Phenomena in Solids*; Oxford University Press: Oxford, 2001.
[32] Bid, A.; Bora, A.; Raychaudhuri, A. K. Temperature dependence of the resistance of metallic nanowires of diameter ≥ 15 nm: Applicability of Bloch-Grüneisen theorem. *Phys. Rev. B* **2006**, *74*, 035426.
[33] Talantsev, E. F. Quantifying the charge carrier interaction in metallic twisted bilayer graphene superlattices. *Nanomaterials* **2021**, *11*, 1306.
[34] Agarwal, T.; Patra, C.; Kataria, A.; Chowdhury, R. R.; Singh, R. P. Quasi-two-dimensional anisotropic superconductivity in Li-intercalated 2H-TaS_2. *Phys. Rev. B* **2023**, *107*, 174509.
[35] Ni, S. L.; Zhou, M. H.; Lin, Z. F.; Ruan, B. B.; Li, Z. F.; Zou, Z. W.; Xu, Z. H.; Ren, Z. A. Crystal growth, superconductivity, and charge density wave of pristine and Pd-intercalated 2H-TaS_2. *Phys. Rev. B* **2023**, *108*, 075103.
[36] Ochoa, H.; Fernandes, R. M. Extended linear-in-T resistivity due to electron-phason scattering in moiré superlattices. *Phys. Rev. B* **2023**, *108*, 075168.
[37] K. P, S.; Gofman, R. A.; Nitzav, Y.; Almoalem, A.; Mangel, I.; Shiroka, T.; Plumb, N. C.; Bigi, C.; Bertran, F.; Sánchez-Barriga, J. et al. Ising superconductivity in the bulk incommensurate layered material $(PbS)_{1.13}(TaS_2)$. *Phys. Rev. B* **2025**, *111*, 054509.
[38] Liu, H. Y.; Li, Y. L.; Ge, J.; Liu, Y. Y.; Liu, S. L.; Wang, H.; Wang, J.; Xing, Y. Transport properties of $(InSe_2)_xNbSe_2$ with enhanced T_c and H_{c2}. *Phys. Rev. B* **2025**, *111*, 094517.
[39] Wilson, A. H. The electrical conductivity of the transition metals. *Proc. R. Soc. London A* **1938**, *167*, 580–593.
[40] Klemm, R. A.; Luther, A.; Beasley, M. R. Theory of the upper critical field in layered superconductors. *Phys. Rev. B* **1975**, *12*, 877–891.
[41] Wawro, A. Superconductivity in Ni/Pb modulated films. *J. Low Temp. Phys.* **1994**, *94*, 351–359.
[42] Tsen, A. W.; Hunt, B.; Kim, Y. D.; Yuan, Z. J.; Jia, S.; Cava, R. J.; Hone, J.; Kim, P.; Dean, C. R.; Pasupathy, A. N. Nature of the quantum metal in a two-dimensional crystalline superconductor. *Nat. Phys.* **2016**, *12*, 208–212.
[43] Falson, J.; Xu, Y.; Liao, M. H.; Zang, Y. Y.; Zhu, K. J.; Wang, C.; Zhang, Z. T.; Liu, H. C.; Duan, W. H.; He, K. et al. Type-II ising pairing in few-layer stanene. *Science* **2020**, *367*, 1454–1457.
[44] Chen, D. Y.; Wu, Y. L.; Jin, L.; Li, Y. K.; Wang, X. X.; Duan, J. X.; Han, J. F.; Li, X.; Long, Y. Z.; Zhang, X. M. et al. Superconducting properties in a candidate topological nodal line semimetal $SnTaS_2$ with a centrosymmetric crystal structure. *Phys. Rev. B* **2019**, *100*, 064516.
[45] Navarro-Moratalla, E.; Island, J. O.; Mañas-Valero, S.; Pinilla-Cienfuegos, E.; Castellanos-Gomez, A.; Quereda, J.; Rubio-Bollinger, G.; Chirolli, L.; Silva-Guillén, J. A.; Agraït, N. et al. Enhanced superconductivity in atomically thin TaS_2. *Nat. Commun.* **2016**, *7*, 11043.
[46] Zheng, G. L.; Xie, W. Q.; Albarakati, S.; Algarni, M.; Tan, C.; Wang, Y. H.; Peng, J. Y.; Partridge, J.; Farrar, L.; Yi, J. B. et al. Gate-tuned interlayer coupling in van der Waals ferromagnet Fe_3GeTe_2 nanoflakes. *Phys. Rev. Lett.* **2020**, *125*, 047202.
[47] Tan, C.; Xie, W. Q.; Zheng, G. L.; Aloufi, N.; Albarakati, S.; Algarni, M.; Li, J. B.; Partridge, J.; Culcer, D.; Wang, X. L. et al. Gate-controlled magnetic phase transition in a van der Waals magnet Fe_5GeTe_2. *Nano Lett.* **2021**, *21*, 5599–5605.

[48] Tan, C.; Liao, J. H.; Zheng, G. L.; Algarni, M.; Lin, J. Y.; Ma, X.; Mayes, E. L.; Field, M. R.; Albarakati, S.; Panahandeh-Fard, M. et al. Room-temperature magnetic phase transition in an electrically tuned van der Waals ferromagnet. *Phys. Rev. Lett.* **2023**, *131*, 166703.

[49] Zheng, G. L.; Tan, C.; Chen, Z.; Wang, M. Y.; Zhu, X. D.; Albarakati, S.; Algarni, M.; Partridge, J.; Farrar, L.; Zhou, J. H. et al. Electrically controlled superconductor-to-failed insulator transition and giant anomalous hall effect in Kagome metal CsV_3Sb_5 nanoflakes. *Nat. Commun.* **2023**, *14*, 678.

[50] Hu, H.; Liu, M.; Wang, Z. F.; Zhu, J. Y.; Wu, D. X.; Ding, H. P.; Liu, Z.; Liu, F. Quantum electronic stress: Density-functional-theory formulation and physical manifestation. *Phys. Rev. Lett.* **2012**, *109*, 055501.

[51] Zhang, X. M.; Zhao, M. W.; Liu, F. Enhancing superconductivity in bulk β-Bi_2Pd by negative pressure induced by quantum electronic stress. *Phys. Rev. B* **2019**, *100*, 104527.

[52] McMillan, W. L. Transition temperature of strong-coupled superconductors. *Phys. Rev.* **1968**, *167*, 331–344.

[53] Allen, P. B.; Dynes, R. C. Transition temperature of strong-coupled superconductors reanalyzed. *Phys. Rev. B* **1975**, *12*, 905–922.

[54] Zhao, K.; Lv, B.; Xue, Y. Y.; Zhu, X. Y.; Deng, L. Z.; Wu, Z.; Chu, C. W. Chemical doping and high-pressure studies of layered β-$PiBi_2$ single crystals. *Phys. Rev. B* **2015**, *92*, 174404.

[55] Schlicht, A.; Schwenker, M.; Biberacher, W.; Lerf, A. Superconducting transition temperature of 2H-TaS_2 intercalation compounds determined by the phonon spectrum. *J. Phys. Chem. B* **2001**, *105*, 4867–4871.

[56] de la Barrera, S. C.; Sinko, M. R.; Gopalan, D. P.; Sivadas, N.; Seyler, K. L.; Watanabe, K.; Taniguchi, T.; Tsen, A. W.; Xu, X. D.; Xiao, D. et al. Tuning Ising superconductivity with layer and spin-orbit coupling in two-dimensional transition-metal dichalcogenides. *Nat. Commun.* **2018**, *9*, 1427.

[57] Hohenberg, P.; Kohn, W. Inhomogeneous electron gas. *Phys. Rev.* **1964**, *136*, B864–B871.

[58] Kohn, W.; Sham, L. J. Self-consistent equations including exchange and correlation effects. *Phys. Rev.* **1965**, *140*, A1133–A1138.

[59] Perdew, J. P.; Burke, K.; Ernzerhof, M. Generalized gradient approximation made simple. *Phys. Rev. Lett.* **1996**, *77*, 3865–3868.

[60] Blöchl, P. E. Projector augmented-wave method. *Phys. Rev. B* **1994**, *50*, 17953–17979.

[61] Klimeš, J.; Bowler, D. R.; Michaelides, A. Chemical accuracy for the van der Waals density functional. *J. Phys. Condens. Matter* **2010**, *22*, 022201.

[62] Wang, V.; Xu, N.; Liu, J. C.; Tang, G.; Geng, W. T. VASPKIT: A user-friendly interface facilitating high-throughput computing and analysis using VASP code. *Comput. Phys. Commun.* **2021**, *267*, 108033.